considerable changes in the framework geometry as confirmed by in situ single-crystal and powder x-ray diffraction measurements. The material is distinct in having a nanoporous host lattice chemistry (pore size, shape, and electronic potential) that may be manipulated in a switchable fashion, in this case by the external stimulation of spin crossover by temperature variation. Conversely, the reversible exchange of guest species has been shown to provide a unique mechanism with which to conveniently perturb the geometry and electronic environment of spin crossover centers, introducing a previously unstudied approach for the systematic investigation of this phenomenon. We note here that the desorption and resorption of guest species promises to provide an additional stimulus for spin crossover, suggesting potential application in areas such as molecular sensing (change in the color, magnetism, size, shape, etc. of the host with guest sorption). In the longer term, it is anticipated that the inclusion of guest and template species with specific electronic functions into molecular lattices that have controllable switching, including communication between these switching centers through coordination linkages, may lead to more advanced materials having other unique and potentially useful physicochemical properties.

References and Notes

1. M. D. Hollingsworth, *Science* **295**, 2410 (2002).
2. J. M. Lehn, *Science* **295**, 2400 (2002).
3. B. F. Hoskins, R. Robson, *J. Am. Chem. Soc.* **112**, 1546 (1990).
4. M. Eddaoudi *et al.*, *Science* **295**, 469 (2002).
5. C. J. Kepert, T. J. Prior, M. J. Rosseinsky, *J. Am. Chem. Soc.* **122**, 5158 (2000).
6. J. S. Seo *et al.*, *Nature* **404**, 982 (2000).
7. M. J. Zaworotko, *Nature* **402**, 242 (1999).
8. A. V. Nossov, D. V. Soldatov, J. A. Ripmeester, *J. Am. Chem. Soc.* **123**, 3563 (2001).
9. P. Gütlich, Y. Garcia, H. A. Goodwin, *Chem. Soc. Rev.* **29**, 419 (2000).
10. S. Decurtins, P. Gütlich, C. P. Köhler, H. Spiering, A. Hauser, *Chem. Phys. Lett.* **105**, 1 (1984).
11. O. Kahn, C. J. Martinez, *Science* **279**, 44 (1998).
12. E. Breuning *et al.*, *Angew. Chem. Int. Ed.* **39**, 2504 (2000).
13. S. Brooker, P. G. Plieger, B. Moubaraki, K. S. Murray, *Angew. Chem. Int. Ed.* **38**, 408 (1999).
14. J. A. Real *et al.*, *Science* **268**, 265 (1995).
15. N. Moliner *et al.*, *Inorg. Chem.* **39**, 5390 (2000).
16. Y. Garcia *et al.*, *Inorg. Chem.* **38**, 4663 (1999).
17. A. Ozarowski, Y. Shunzhong, B. R. McGarvey, A. Mislankar, J. E. Drake, *Inorg. Chem.* **30**, 3167 (1991).
18. Y. Garcia *et al.*, *Chem. Mater.* **10**, 2426 (1998).
19. O. Roubeau, J. G. Haasnoot, E. Codjovi, F. Varret, J. Reedijk, *Chem. Mater.* **14**, 2559 (2002).
20. T. Kitazawa *et al.*, *J. Mater. Chem.* **6**, 119 (1996).
21. V. Niel, J. M. Martinez-Agudo, M. C. Muñoz, A. B. Gaspar, J. A. Real, *Inorg. Chem.* **40**, 3838 (2001).
22. **1·(EtOH)**: $C_{46}Fe_2H_{38}N_{20}O_1S_4$, M = 1126.88, monoclinic, $C2/c$. For T = {150(2), 25(2)} K: a = {17.838(4), 17.803(6)}; b = {30.694(6), 30.608(10)}; c = {20.042(4), 19.843(6)} Å, β = {90.016(4), 90.124(5)}, V = {10973(4), 10813(6)} Å^3, Z = 8, μ(Mo-Kα) = {0.735, 0.746} mm^{-1}. Data were collected on two separate crystals on a Bruker Smart 1000 CCD equipped with Mo-K$_\alpha$ (λ = 0.71073 Å) radiation and Oxford Instruments nitrogen gas and helium gas cryostreams. Full-matrix least squares refinement on F_o^2 converged to $R1$ = {0.0582, 0.0924}, $wR2$ = {0.1118, 0.2179}. [See (*35*) for details.]
23. M. Kondo *et al.*, *Chem. Mater.* **12**, 1288 (2000).
24. **1**: $C_{22}Fe_1H_{16}N_{10}S_2$, M = 540.04, orthorhombic, *Ibam*, a = 8.418(19), b = 16.70(4), c = 20.62(5) Å, V = 2899(12) Å^3, T = 375(2) K, Z = 4, μ (Mo-Kα) = 0.692 mm^{-1}. Full matrix least-squares refinement on F_o^2 converged to $R1$ = 0.1143, $wR2$ = 0.2447. [See (*35*) for details.]
25. D. R. Corbin *et al.*, *J. Am. Chem. Soc.* **112**, 4821 (1990).
26. J. L. Atwood, J. E. D. Davies, D. D. MacNicol, F. Vögtle, Eds., *Comprehensive Supramolecular Chemistry* (Pergamon Press, New York, 1996), vol. 6.
27. O. Kahn, J. Larionova, J. V. Yakhmi, *Chem. Eur. J.* **5**, 3443 (1999).
28. C. J. Kepert, D. Hesek, P. D. Beer, M. J. Rosseinsky, *Angew. Chem. Int. Ed.* **37**, 3158 (1998).
29. C. J. Kepert, M. J. Rosseinsky, *Chem. Commun.* **1999**, 375 (1999).
30. H. Li, M. Eddaoudi, M. O'Keeffe, O. M. Yaghi, *Nature* **402**, 276 (1999).
31. K. Biradha, Y. Hongo, M. Fujita, *Angew. Chem. Int. Ed.* **39**, 3843 (2000).
32. B. F. Abrahams, P. A. Jackson, R. Robson, *Angew. Chem. Int. Ed.* **37**, 2656 (1998).
33. Powder x-ray diffraction measurements were made in situ during guest desorption and resorption under controlled environment (temperature and vapor) conditions. Refined unit cells for the resorbed phases at 303 K: **1·(EtOH)**, a = 18.041(3), b = 31.174(4), c = 19.908(6) Å, β = 90.28(3); **1·(MeOH)**, a = 17.987(3), b = 31.132(4), c = 19.851(6) Å, β = 89.98(3); **1·(PrOH)**, a = 18.12(2), b = 31.27(3), c = 19.85(4) Å, β = 89.8(2). [See (*35*) for details.]
34. The observed decrease in the Fe2-N bond lengths of ca. 0.07 Å is lower than the 0.1 to 0.2 Å expected for spin crossover in Fe(II) (*9*) and may reflect a degree of trapping of the high-spin state at the Fe2 site caused by the quench-cooling of the crystal to 25 K.
35. Single-crystal and powder XRD data, thermogravimetric analyses, magnetic data, Mössbauer data are available (see Materials and Methods, SOM Text, figs. S1 to S9, and tables S1 to S20). Crystallographic data were deposited in the Cambridge Crystallographic Database Centre [**1·(EtOH)** (150 K): CCDC-189340; **1·(EtOH)** (25 K): CCDC-189341; **1** (375 K): CCDC-189342].
36. Supported by the Australian Research Council (C.J.K. and K.S.M.).

Supporting Online Material

www.sciencemag.org/cgi/content/full/298/5599/1762/DC1
Materials and Methods
SOM Text
Figs. S1 to S9
Tables S1 to S20

10 July 2002; accepted 25 October 2002

Seismotectonics of Mid-Ocean Ridge Propagation in Hess Deep

Jacqueline S. Floyd,[1,2]* Maya Tolstoy,[2] John C. Mutter,[1,2,3] Christopher H. Scholz[1,2]

Hydroacoustic data from the eastern equatorial Pacific reveal low-magnitude seismicity concentrated at the propagating tip of the Galapagos Rise in Hess Deep. The patterns of seismicity and faulting are similar to those observed in the process zone of laboratory-scale propagating tensile cracks. Because the fracture energy required for propagation scales with crack length and process zone size, it follows that ridges can propagate stably in the brittle crust without exceptional resisting forces as proposed by previous models based on linear elastic fracture mechanics.

Lithospheric rifting and mid-ocean ridge propagation are the processes by which ocean basins are formed on Earth. Ridge propagation traditionally has been studied using the linear elastic fracture mechanics (LEFM) approach, in which the ridge is idealized as a tensile crack in an elastic plate and propagation occurs when the stress at the tip reaches a critical value (*1–3*). Few studies of ridge propagation have relied on earthquake data, because ridge earthquake magnitudes typically lie below the ~4.5 moment magnitude (M_w) detection threshold of teleseismic networks. Hydroacoustic monitoring in the eastern equatorial Pacific Ocean (*4*), however, has recently provided long-term records of low-magnitude (M_w ~ 1.8 to 4.4) seismicity at the propagating tip of the Galapagos Rise in Hess Deep (Fig. 1). We present observations of hydroacoustic seismicity and faulting in Hess Deep, which provide an opportunity to study the dynamics of ridge propagation and to test models based on the LEFM approach.

The Galapagos Rise is an intermediate-rate (4.5 to 6.0 cm/year full rate) spreading center that is propagating at ~6.5 cm/year (*5*) into oceanic crust 300,000 to 1 million years old accreted at the fast-spreading (13.5 cm/year full rate) East Pacific Rise (EPR). Regionally, the Galapagos Rise and EPR form a triple junction; however, multibeam bathymetry data show that the two ridges do not intersect (*6*) (Figs. 1 and 2). The Galapagos Rise volcanic ridge is identified as an elongate bathymetric high that reaches ~15 km into the 5.4-km-deep Hess Deep rift (Fig. 2). Hess Deep is bounded by two major normal faulted margins and contains a northward-

[1]Department of Earth and Environmental Sciences, [2]Lamont-Doherty Earth Observatory, [3]Earth Institute, Columbia University, 61 Route 9W, Palisades, NY 10964, USA.

*To whom correspondence should be addressed. E-mail: jsfloyd@ldeo.columbia.edu

tilted fault block, 25 km long by 8 km wide, known as the intrarift ridge (*7, 8*). Thin sediment cover (<10 to 20 m) has left rift structures well exposed (*9*). Lithospheric extension has exposed sheared and serpentinized gabbro and peridotites along the rift valley walls (*7, 8, 10, 11*) and has produced an asymmetric morphology that is similar to continental rifts (*5, 8*). Flexurally uplifted rift shoulders define the boundaries of Hess Deep and extend eastward along the triangular region of rough crust known as the Galapagos Gore (*12*) (Fig. 1A). The gore margins are lined by depressions that may be remnants of prior Hess Deep–like grabens (*7*), suggesting that the Hess Deep rift is a steady-state structure at the tip of the propagating ridge.

Hydroacoustic data were acquired with an array of six autonomous moored hydrophones deployed in May 1996 (*4, 13, 14*) (Fig. 1). More than 200 hydroacoustic events were recorded in Hess Deep from May 1996 to October 2000. Earthquake magnitudes in Hess Deep range from the minimum hydroacoustic detection threshold of $M \sim 1.8$ to 2.2 (*4, 15*) up to a body wave magnitude (m_b) of 3.5 to 4.4 determined by teleseismic data. The rate of Hess Deep seismicity was steady and averaged 0.14 events/day (*16*). One m_b = 4.4 mainshock-aftershock sequence was detected on 28 August 1998 on the northwest margin of Hess Deep (Fig. 2). A focal mechanism was not obtained; however, the sequence lies near a teleseismically recorded 1989 M_w = 5.3 strike-slip earthquake (*17*) that has a 343°N left-lateral strike-slip nodal plane that nearly parallels the 350°N trend of the Pacific-Cocos ridge, which suggests that it may have reactivated an abyssal hill fault. The unusually large magnitude of the 1998 mainshock, its location outside of the Hess Deep rift, and its proximity to the 1989 event suggest that the 1998 sequence may also have been a strike-slip event.

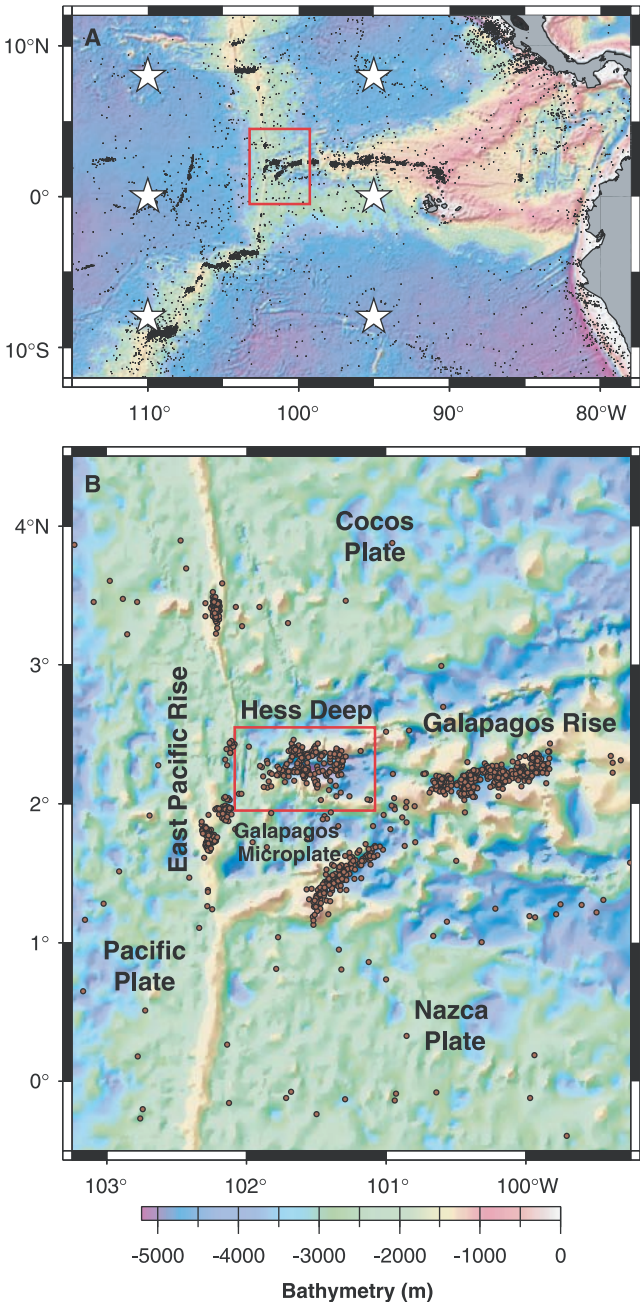

Fig. 1. (**A**) Bathymetry and hydroacoustic seismicity (black dots) of the eastern equatorial Pacific (*4, 32*). The Galapagos Gore is the westward-pointing triangular region of elevated seafloor. Stars mark hydrophone locations (*4*). The red box in (A) outlines the map (**B**) of the Galapagos triple junction. The red box in (B) outlines the map of Hess Deep (Fig. 2).

Seismicity at Hess Deep is diffuse ≤ 20 km west of the rift, where EPR crust is undergoing initial brittle extension, and reaches a maximum density at the base of the rift (Figs. 2 and 3). The seismicity trends east-west along the central rift axis and north of the intrarift ridge, and abruptly ends at 101°17′W. East of 101°17′W, seismicity clusters along the ridge and transform faults but is absent along the boundaries of the gore (Fig. 1). Some seismicity in Hess Deep may be due to magmatism; however, time-series analysis (*16*) does not reveal swarm activity that is characteristic of magmatic events.

Focal mechanisms cannot be obtained from hydroacoustic data; however, we can better understand the seismicity patterns and the possible faulting mechanisms by calculating the Coulomb stress change due to extension at the Galapagos Rise (*18–22*) (Fig. 4). We modeled the Galapagos Rise and EPR as tensile cracks located at 1 km depth in an elastic half-space and calculated the dilatational strain and static stress change for normal and strike-slip faults due to opening by an amount equal to a typical dike width of 1 m (*23*). The tip of the Galapagos Rise is placed at the base of the rift tip depression (Fig. 4A), where the lithosphere has extended sufficiently for extrusive volcanism to begin. Dilatational strain reaches ≤ 20 km directly west of the crack tip and extends at angles of ±60° toward the EPR (Fig. 4B). Similarly, bathymetry data show deformation ≤ 20 km west of Hess Deep and a V-shaped depression opening westward at the leading edge of Hess Deep (Fig. 4A). Coulomb stress changes indicate regions where optimally oriented normal and strike-slip faults are brought closer to or further away from failure (Fig. 4, C and D). The maximum stress increase for strike-slip faults forms two broad lobes west of the rift tip. Left-lateral strike-slip faulting on north-south–oriented planes is promoted at the location of the 1989 strike-slip event and the 1998 mainshock-aftershock sequence northwest of Hess Deep (Fig. 4, A and C), which supports our interpretation that these two events ruptured abyssal hill faults by left-lateral motion. The stress increase for normal faults is greatest ≤ 20 km west of the rift and decreases to the east (Fig. 4D), which is consistent with the high concentration of seismicity at the rift tip depression and an

eastward decrease in seismicity (Fig. 3, C and D).

The spatial correlation between the Coulomb stress change models and the Hess Deep seismicity supports the model of the Galapagos Rise as an elastic tensile crack. The elastic assumption is applicable except at the immediate crack tip, where LEFM predicts an elliptical displacement taper and a stress singularity, which cannot be sustained in materials with finite yield strength (*24, 25*). Distributed faulting and seismicity in Hess Deep and a linear taper in seafloor displacement (dipping ~14°) between the EPR crust and the rift tip depression (Fig. 3D) are direct indicators of inelastic deformation at the rift tip (*26*).

Acoustic emission studies show that crack growth is controlled by a sequence of microcracking in the process zone, followed by coalescence and nucleation of the next increment of the propagating crack (*27, 28*). We recognize analogs of the three phases of microcracking, nucleation, and propagation in the spatial distribution of seismicity and faulting in Hess Deep (Fig. 3, C and D). Ridge propagation at the Galapagos Rise begins by loading the EPR crust under tensile stress and inducing fracturing and seismicity west of Hess Deep (Figs. 2 and 3). The fractures dilate under low confining pressures of the shallow crust and enhance one another until they coalesce and nucleate crustal-scale normal faults (*28*). The nucleation phase is expressed in Hess Deep by an increase in seismicity and large-offset normal faulting to the base of the rift (Fig. 3, C and D). Magma rises through the rift floor as the ridge propagates, and seismicity continues until crustal extension is taken up entirely by seafloor spreading. The advancing ridge then bisects the rift, and each half is rafted toward the margins to form the depressions preserved along the boundary of the Galapagos Gore.

Hydroacoustic and morphologic evidence for process zone deformation in Hess Deep is inconsistent with LEFM models. We use the Griffith energy balance approach and consider the thermodynamic equilibrium between the mechanical work supplied and the energy consumed by the crack surface area (*29*). The original Griffith formulation assumes that all of the mechanical energy goes into the crack surface area. At equilibrium, the critical failure stress σ_f at which the crack will propagate is related to the crack half-length c by

$$\sigma_f = (2E\gamma/\pi c)^{1/2} \quad (1)$$

where E is Young's modulus and γ is the specific surface energy, the energy per unit area required to break atomic bonds (*30*). This equation shows that σ_f decreases with c and defines a point of unstable equilibrium at

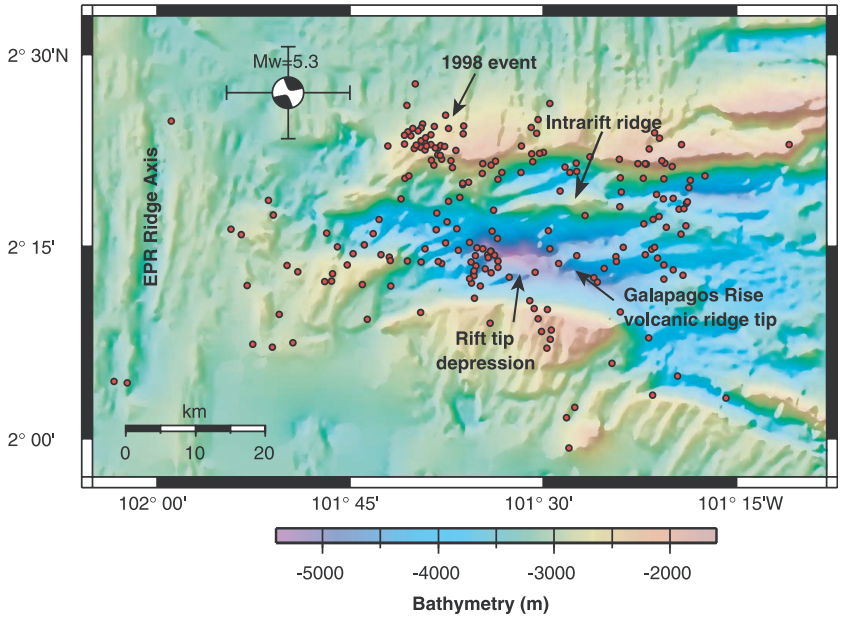

Fig. 2. Bathymetry and hydroacoustic seismicity (red circles) (*4*) in Hess Deep. Multibeam bathymetry data are combined with predicted bathymetry from satellite altimetry measurements (*32*). The focal mechanism for the 1989 M_w = 5.3 strike-slip earthquake is plotted with location error bars (*17*).

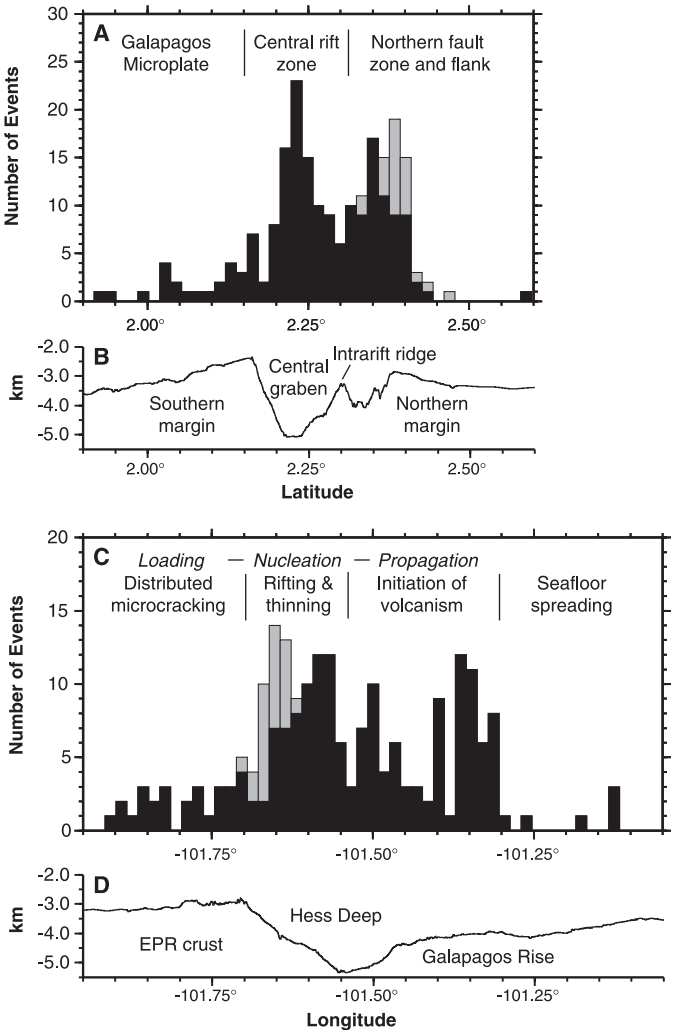

Fig. 3. Histograms showing the number of hydroacoustic events per minute of latitude (**A**) and longitude (**C**), with bathymetry profiles (**B** and **D**). Aftershocks from the 1998 mainshock-aftershock sequence are separated from the total earthquake population (gray bars). We recognize three phases of rifting and ridge propagation, as labeled in (C).

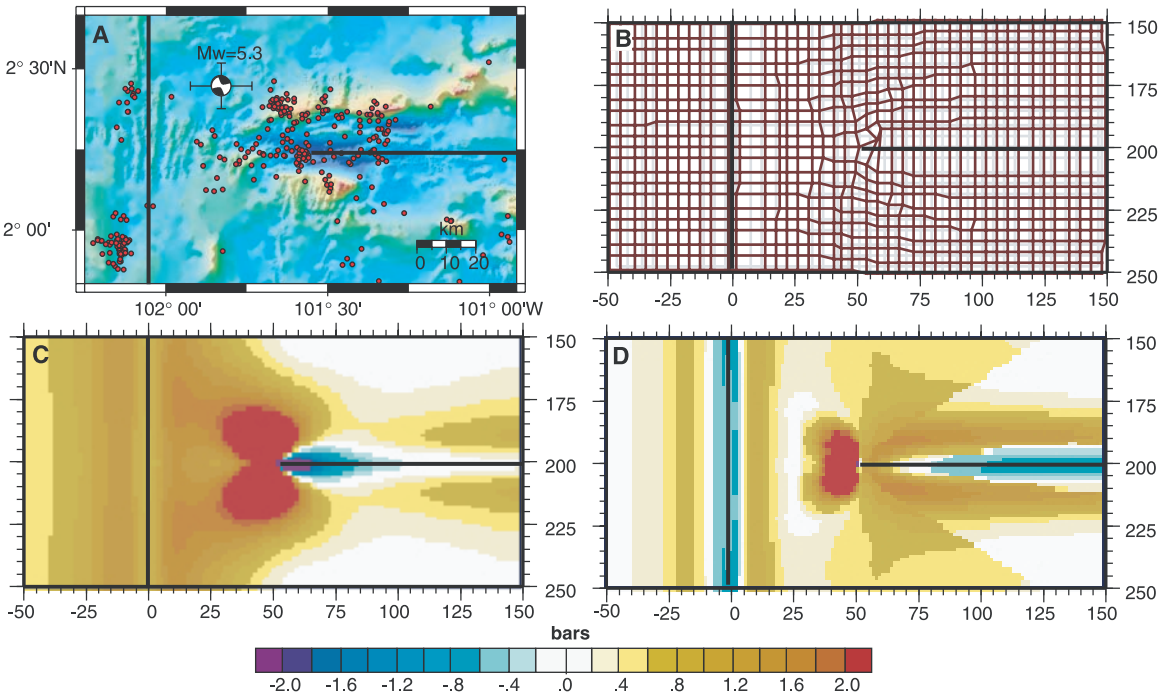

Fig. 4. Dilatational strain magnified 10,000 times (**B**) and Coulomb stress change for optimally oriented strike-slip (**C**) and normal (**D**) faults in response to 1 m of opening at the Galapagos Rise and EPR (**A**). Hydroacoustic events (red circles, A) that lie within regions of stress increase for strike-slip (C) and normal (D) faults are likely to have strike-slip and normal faulting mechanisms, respectively. The axes of (B), (C), and (D) are in units of kilometers.

which the crack will propagate catastrophically without limit. Studies of fault scaling relationships show that the work of lengthening the crack, expressed as the fracture energy G, increases linearly with c (*24, 25, 30, 31*). The dependence of G on c means that γ is not a constant, as assumed by Griffith (*29*), but scales with c:

$$G = 2\gamma = \zeta c \qquad (2)$$

(*30*), where ζ is a function of lithology and confining pressure (*30, 31*). Hence, the critical failure stress

$$\sigma_f = (E\zeta/\pi)^{1/2} \qquad (3)$$

is independent of c, and the crack may propagate stably. Energy originally thought to be driving runaway crack growth is actually creating microcracks within the process zone. Vermilye and Scholz (*31*) showed that process zone width scales linearly with c, which is evidence that G scales with c (*30*).

Previous investigators using the LEFM approach proposed that a viscous suction force due to reduced asthenospheric upwelling limited the ridge propagation rate (*2, 33*). In addition to its analytical appeal, the viscous suction mechanism provided an explanation for the rift tip depression (*2, 33*). Equation 3 shows, however, that neither viscous suction nor any other boundary conditions are necessary for stable propagation. The rift tip depression in Hess Deep may form simply by normal faulting and thinning of the EPR crust during the nucleation phase. Asthenospheric flow at the ridge tip may actually promote propagation by thermally weakening the crust (*34*) and driving hydrothermal circulation to create serpentinized shear zones that line the Hess Deep rift (*35, 36*).

References and Notes

1. R. N. Hey, F. K. Duennebier, W. J. Morgan, *J. Geophys. Res.* **85**, 2647 (1980).
2. J. Phipps Morgan, E. M. Parmentier, *J. Geophys. Res.* **90**, 8603 (1985).
3. K. C. Macdonald, D. Scheirer, S. M. Carbotte, *Science* **253**, 986 (1991).
4. C. G. Fox, H. Matsumoto, T.-K. A. Lau, *J. Geophys. Res.* **106**, 4183 (2001).
5. P. Lonsdale, *J. Geophys. Res.* **93**, 13511 (1988).
6. R. C. Searle, J. Francheteau, *Mar. Geophys. Res.* **8**, 95 (1986).
7. R. N. Hey, K. S. Deffeyes, G. L. Johnson, A. Lowrie, *Nature* **237**, 20 (1972).
8. J. Francheteau *et al.*, *Earth Planet. Sci. Lett.* **101**, 281 (1990).
9. L. P. Zonenshain, L. I. Kogan, L. A. Savostin, A. J. Golmstock, A. M. Gorodnitskii, *Mar. Geol.* **37**, 209 (1980).
10. J. A. Karson *et al.*, *G-Cubed* **3**, 2001GC000155 (2002).
11. C. Mevel, K. M. Gillis, S. S. Party, *Proc. Ocean Drill. Prog. Init. Rep.* **147**, 5 (1993).
12. J. C. Holden, R. S. Dietz, *Nature* **235**, 266 (1972).
13. Hydroacoustic, or tertiary (*T*), waves are formed by conversion of elastic waves to acoustic waves at the seafloor (*14*). *T* waves transmit energy over thousands of kilometers through the oceanic sound channel with very little attenuation. *T* waves do not provide earthquake depth or focal mechanism information and may be blocked by bathymetry. Location errors are ~2 km within Hess Deep. The array located seismic events within the 5.4-km-deep rift as well as the rift shoulders, which suggests that the Hess Deep earthquake locations have not been biased by bathymetry.
14. I. Tolstoy, M. Ewing, *Bull. Seismol. Soc. Am.* **40**, 25 (1950).
15. D. R. Bohnenstiehl, M. Tolstoy, R. P. Dziak, C. G. Fox, D. K. Smith, *Tectonophysics* **354**, 49 (2002).
16. See supporting data on *Science* Online.
17. A. M. Dziewonski, G. Ekstrom, J. H. Woodhouse, G. Zwart, *Phys. Earth Planet. Inter.* **62**, 185 (1990).
18. The elastic dislocation modeling code, available from Ross Stein (http://quake.wr.usgs.gov), is based on the codes of Okada (*19*) and Crouch and Starfield (*20*). Poisson's ratio is 0.25, the effective friction coefficient is 0.4, and Young's modulus is 8.0×10^{10} Pa. Stress and strain fields are plotted at 7.5 km depth.
19. Y. Okada, *Bull. Seismol. Soc. Am.* **82**, 1018 (1992).
20. S. L. Crouch, A. M. Starfield, *Boundary Element Methods in Solid Mechanics* (Allen Unwin, London, 1983).
21. G. C. P. King, R. S. Stein, J. Lin, *Bull. Seismol. Soc. Am.* **84**, 935 (1994).
22. S. Toda, R. S. Stein, *Geophys. Res. Lett.* **27**, 2301 (2000).
23. J. R. Delaney *et al.*, *Science* **281**, 222 (1998).
24. P. A. Cowie, C. H. Scholz, *J. Struct. Geol.* **14**, 1133 (1992).
25. ———, *J. Struct. Geol.* **14**, 1149 (1992).
26. N. H. Dawers, M. H. Anders, C. H. Scholz, *Geology* **21**, 1107 (1993).
27. D. A. Lockner, J. D. Byerlee, V. Kuksenko, A. Ponomarev, A. Sidorin, *Nature* **350**, 39 (1991).
28. Z. Reches, D. A. Lockner, *J. Geophys. Res.* **99**, 18159 (1994).
29. A. A. Griffith, *Philos. Trans. R. Soc. London* **221**, 163 (1920).
30. C. H. Scholz, *The Mechanics of Earthquakes and Faulting* (Cambridge Univ. Press, New York, ed. 2, 2002).
31. J. M. Vermilye, C. H. Scholz, *J. Geophys. Res.* **103**, 12223 (1998).
32. W. H. F. Smith, D. T. Sandwell, *Science* **277**, 1956 (1997).
33. E. M. Parmentier, G. Schubert, *Geophys. Res. Lett.* **16**, 183 (1989).
34. W. R. Buck, F. Martinez, M. S. Steckler, J. R. Cochran, *Tectonics* **7**, 213 (1988).
35. W. Schmitz, A. Singer, H. Backer, P. Stoffers, *Mar. Geol.* **46**, M17 (1982).
36. J. S. Floyd, J. C. Mutter, A. M. Goodliffe, B. Taylor, *Nature* **411**, 779 (2001).

37. We thank R. Buck, C. Fox, and D. Bohnentiehl for early reviews of the manuscript; C. G. Fox and NOAA for hydroacoustic data; and G. Christeson and NOAA–National Geophysical Data Center for bathymetry data. Supported by NSF grants OCE 01-18568 (J.C.M., J.S.F.) and OCE-9812237 (M.T.). This is LDEO contribution no. 6395.

Supporting Online Material

www.sciencemag.org/cgi/content/full/298/5599/1765/DC1

Fig. S1

30 August 2002; accepted 5 November 2002